J. Mech. Phys. Solids 181 (2023) 105467

Contents lists available at ScienceDirect

Journal of the Mechanics and Physics of Solids

journal homepage: www.elsevier.com/locate/jmps

What are the “dispersive shear bands” on the surfaces of layered heterostructured materials?

Huwen Ma [a,b], Yanchun Zhao [a,b,*], Zhi Lyu [a,b], Xue Wang [d], Yuntian Zhu [c,*], Yanfei Gao [d,*]

[a] State Key Laboratory of Advanced Processing and Recycling of Non-Ferrous Metals, Lanzhou University of Technology, Lanzhou 730050, PR China
[b] Wenzhou Pump and Valve Engineering Research Institute, Lanzhou University of Technology, Wenzhou 325105, PR China
[c] Department of Materials Science and Engineering, City University of Hong Kong, Hong Kong 999077, PR China
[d] Department of Materials Science and Engineering, University of Tennessee, Knoxville, TN 37996, USA

ARTICLE INFO

Keywords:
Layered heterostructured materials
Necking analysis
“Shear bands” arrangements
Strength-ductility trade-off
3D finite element simulations

ABSTRACT

Hetero-deformation-induced (HDI) strengthening mechanism has been well investigated in heterostructured materials including layered/gradient materials prepared by surface attrition or other processing techniques. While the roles played by the geometrically necessary dislocations (GNDs) and the forward/back stresses on the grain scale have been a focus in nearly all these studies, some latest works reveal the peculiar formation of “dispersive shear bands” or strain localizations on the surfaces of layered/gradient materials. Feature sizes of these “shear bands” are commensurate with the macroscopic sample size, but not on the microstructural length scales, thus excluding the HDI strengthening as the primary mechanism. In this work, using a sandwich structure as an illustrative example, we demonstrate that the origin of these shear bands be localized necking with intermediate wavelengths and inclined orientations, which are critically dictated by the hardening behavior of the constituent layers, the geometric parameters, and the initial morphological perturbations. The layered structure under tension may not neck with an infinite wavelength (i.e., the Considère mode), but neck at intermediate wavelengths which actually correspond to a much larger uniform ductility than the commonly observed Considère necking mode. The arrangements of these shear bands can be further classified as I, X, and W types. Findings in this work not only resolve the origin of recent unusual experimental observations, but also suggest an alternative way of understanding and improving the ductility in heterostructured materials.

1. Introduction

Heterostructured materials have been found to possess simultaneously high strength and good ductility (or more precisely, the uniform elongation and the critical strain at failure), and therefore they have received tremendous research attentions in recent decades (Zhao et al., 2006; Fang et al., 2011; Lu, 2014; Zeng et al., 2016; Wang et al., 2017; Li et al., 2017; Huang et al., 2018; Zhu and Wu, 2019; Li et al., 2020; Zhu and Wu, 2022; Wan et al., 2021; Jiang et al., 2022). The currently reached consensus is that plastic deformation in heterogeneous structures, as exemplified by the hard/soft grain samples shown in Fig. 1(a), is incompatible.

* Corresponding authors.
E-mail addresses: zhaoyanchun@lut.edu.cn (Y. Zhao), y.zhu@cityu.edu.hk (Y. Zhu), ygao7@utk.edu (Y. Gao).

https://doi.org/10.1016/j.jmps.2023.105467
Received 25 June 2023; Received in revised form 3 September 2023; Accepted 14 October 2023
Available online 15 October 2023

Stress/plastic strain gradients occur around the interfaces of the soft/hard layers, necessitating the accommodation of a large number of geometrically necessary dislocations (GNDs). To counteract the accumulation of GNDs in slip systems, the generation of self-stresses and interactions lead to the formation of back stresses. These back stresses contribute to heterogeneity-induced deformation (HDI) strengthening and hardening (Zhu and Wu, 2022; Wan et al., 2021; Jiang et al., 2022). Plenty of crystal plasticity modeling and discrete dislocation plasticity simulations have been conducted, and the main idea on the above microscopic mechanisms has been well validated from both extensive experimental and modeling studies.

An intriguing observation has been found in a number of recent works on heterostructured materials (e.g., gradient nano-grained materials, layered heterostructured materials, polycrystals with bimodal grain size distributions, and others) (Yuan et al., 2019; Wang et al., 2019; Wang et al., 2020; Wang et al., 2020), in which the strain fields are found to show distinctive localization into narrow bands. For example, bi-modal polycrystalline Cu can be manufactured by multiple rounds of equal channel pressing, followed by rolling and annealing, as shown in Fig. 1(b) (Wang et al., 2017). The optical micrographs and grain size distribution plots clearly show the tunability of the coarse-grain vs nano-grain fractions, and the surface strain measurements by digital image correlation (DIC) exhibit localization bands on the same scale as the microstructure. In another example, a dog-bone plate sample was treated by shot peening on both side surfaces, thus generating two surface nanocrystalline layers with a coarse-grained core layer, as shown by Fig. 1 (c) (Wang et al., 2020; Wang et al., 2020). The resulting tensile strain field on the surface obtained by DIC shows significant fluctuations as the macroscopic strain increases. These localized strain bands are inclined and at an angle of roughly 50° to the loading axis, very close to the principal shear direction. Therefore, they are commonly referred to as "shear bands" in the experimental community.* For the strain bands observed on the grain scale (e.g., Fig. 1(b)), the strain localization process may be just slip bands or associated with one or multiple GND pileups, the understanding of which nevertheless makes an auxiliary contribution to the understanding of HDI strengthening mechanism. In contrast, strain localization in Fig. 1(c) takes place at the macroscopic millimeter scale, which is many orders of magnitude larger than the nanocrystalline grain size. The vast difference in length scales suggests that these dispersive shear bands and HDI strengthening mechanism may not have a direct correlation. A question that naturally arises is what mechanisms are governing the initiation and growth of these dispersive shear bands like those in Fig. 1(c). It should be noted that strain localization is normally a consequence of material instability, i.e., the loss of ellipticity or stability of the constitutive response of the stressed material. Typical reasons include strain softening, thermal softening, and non-associate flow (or called flow non-normality), among many others (Rudnicki and Rice, 1975; Needleman, 1988; Gao et al., 2011; Jia et al., 2018). However, none of these common reasons seems to be plausible for the sandwich structure in Fig. 1(c).

If the observed dispersive shear bands are not from material instability, would they be a consequence of geometric instability? We now address this issue from three aspects below. *First*, the textbook interpretation of ductility invokes the onset of the Considère necking condition, followed by void nucleation, growth, and coalescence in the triaxially stressed neck, and the eventual fracture thereof. The Considère criterion relates the strain hardening factor, H, at a given strain rate, $\dot{\varepsilon}$, to the flow stress, σ, by

$$H \equiv \left.\frac{d\sigma}{d\varepsilon}\right|_{\dot{\varepsilon}} = \sigma \tag{1}$$

where σ is true stress and ε is true strain. According to this criterion, delaying the appearance of necking could be obtained by substantially increasing the $d\sigma/d\varepsilon$ (e.g., the most effective ways including phase transformation, lamellae, and heterostructured materials). Meanwhile, the ductility can be described by the uniform ductility (i.e., the critical strain at which necking starts to take place) and the final ductility (i.e., the elongation to failure). Additionally, the ductility is strongly affected by some other materials or geometry related factors such as strain rate sensitivity and initial perturbations (Hutchinson and Neale, 1977; Zhang et al., 2020). Needless to say, the observations in Fig. 1(c) do not correspond to the Considère necking because of their localized nature. *Second*, for plate materials under tension, the necking process can be classified as diffuse necking (i.e., occurring at the initial stage of necking and in a sub-stable flow state) and the localized necking (i.e., occurring in the latter stages of necking, focused on a narrow area and in an unstable flow state), as shown in Fig. 1(d). The plate sample in diffuse necking involves contraction in both thickness and width directions, whereas in localized necking the specimen only contracts in the thickness direction. The localized necking process produces a sharp area of contraction at a characteristic angle to the tension axis, and this angular dependence is well documented in the study of forming limit diagram (Marciniak and Kuczyński, 1969; Wang et al., 2011; Srivastava et al., 2016). Although the inclined angle could resemble those in Fig. 1(c), there is usually an individual localized necking in plate forming, just like the Considère necking case. *Third*, a less known necking analysis involves the periodic necking with variable wavelength (Hill and Hutchinson, 1975; Stören and Rice, 1975; Wang et al., 2021). At one extreme, the surface perturbation is of long wavelength, thus reaching the Considère condition. At the other extreme, an extremely short-wavelength perturbation resembles the Rayleigh surface wave of the open channel flow problem in fluid dynamics, and the resulting uniform ductility is determined by Hill and Hutchinson (Hill and Hutchinson, 1975) as

$$\varepsilon_{uniform}^{Rayleigh} - \varepsilon_{uniform}^{Rayleigh} exp\left(2\varepsilon_{uniform}^{Rayleigh}\right) = N \tag{2}$$

where N is the work hardening exponent during uniaxial tension, and $\varepsilon_{uniform}^{Rayleigh}$ is the uniform ductility of the Rayleigh mode which can

* As explained shortly in this paragraph, we are clearly aware that "shear bands" are strain localizations that usually arise from constitutive instabilities. The reason for the retainment of "dispersive shear bands" is that this is the terminology used in experimental community, and the objective of this work is to explain that these are actually diffuse necking with variable wavelengths.

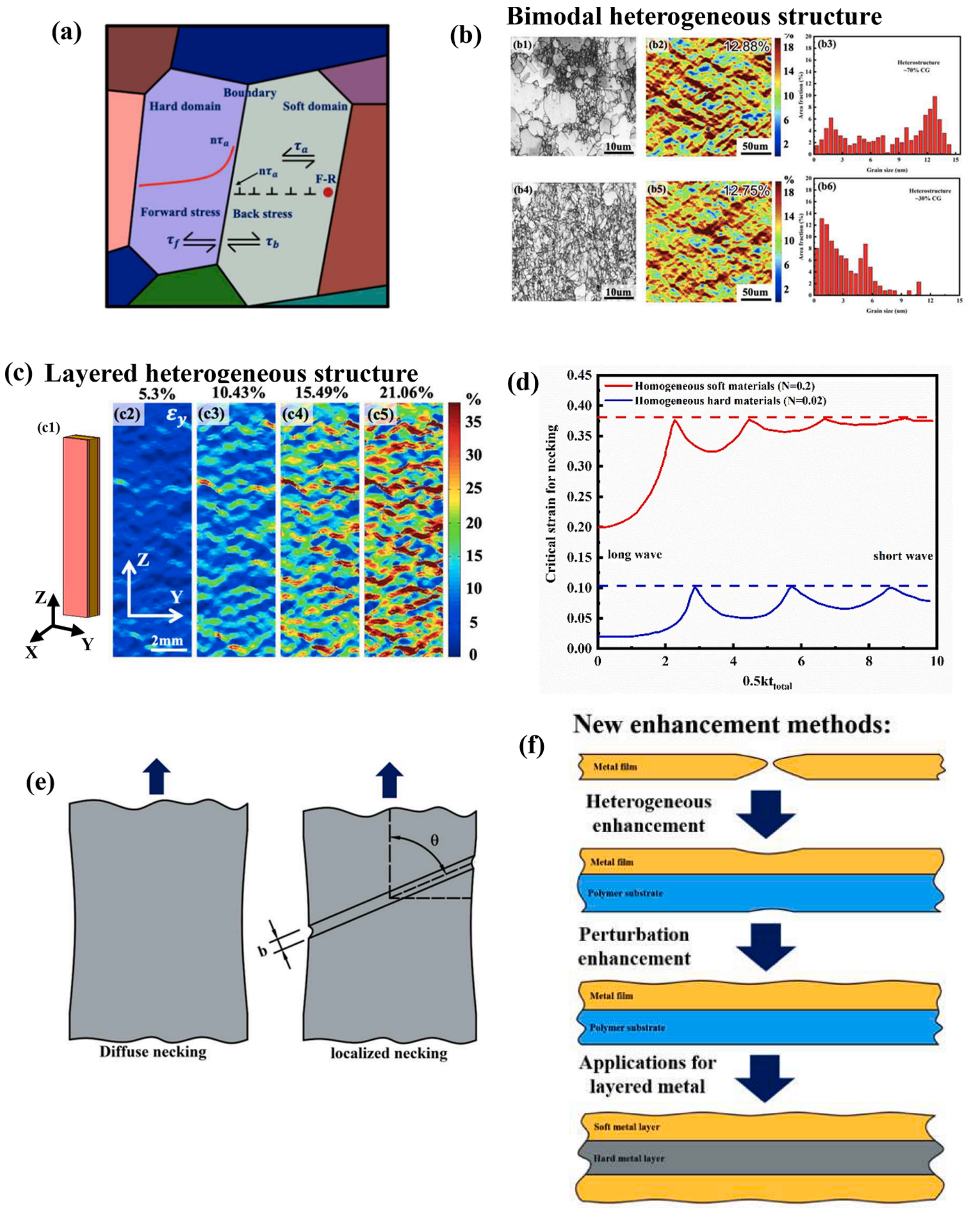

Fig. 1. (a) Schematic diagram of geometrically necessary dislocations (GNDs) being accumulated near the boundary of hard and soft grains, where back/forward stresses are generated in the hard and soft grains, respectively (Zhu and Wu, 2019). (b) The measured strain contours on the surface of the bimodal heterostructured microstructure showing the localized strain bands, with 70 % coarse-grained and 30 % ultrafine-grained Cu in (b1)-(b3), and with 30 % coarse-grained and 70 % ultrafine-grained Cu in (b4)-(b6) (Huang et al., 2018). (c) Surface strain measurements in Ni with surface nanograined structure and coarse-grained core, with respect to the increase of the applied strain level (Wang et al., 2020). (d) Diagram of diffuse necking and localized necking during uniaxial tension of a thin plate, where diffuse necking involves contraction in both the width and thickness directions, but localized necking involves contraction only in the thickness direction and the formation of a sharp neck with a characteristic angle. (e) Theoretical results for homogeneous hard (e.g., $N = 0.02$) and soft (e.g., $N = 0.2$) materials, as obtained by solving the eigenvalue problem for the instability of the deformation field (Wang et al., 2021). (f) Schematic of design ideas for layered heterogeneous material, inspired by the method used to prevent early necking in flexible electronics (Li et al., 2004; Li et al., 2005; Xiang et al., 2005; Li and Suo, 2006; Lu et al., 2010; Jia and Li, 2013; Jia and Li, 2019).

be approximated as $\sqrt{N/2}$ by solving the above equation. As shown in Fig. 1(e), the critical necking strain curves for homogeneous materials with work hardening exponent equal to 0.2 (an example value for a soft material) and to 0.02 (an example value for a hard material) are obtained by solving the eigenvalue problem that governs the stability of the boundary value problem. For intermediate wavelengths, the solution is not monotonic, but the Considère and Rayleigh solutions prescribe the lower and upper bounds, respectively. Additionally, short wavelength necking could lead to a ductility that is much higher than the Considère necking condition. As shown in our previous work (Wang et al., 2021), these analytical solutions can only be reproduced in finite element simulations with an extremely small amplitude of initial perturbation. Nevertheless, it is likely that the experimental observations in Fig. 1(c) could result from intermediate-wavelength necking, although this does not occur in homogeneous materials.

The present work is based on two hypotheses that give a completely novel perspective to the "dispersive shear bands" in Fig. 1(c) and ductility enhancement in layered heterostructured materials. The above discussions of Considère necking, plate/sheet forming limit diagram, and variable-wavelength necking provide the essential mechanics background for the types and critical conditions for the onset of nonuniform deformation. Our *first hypothesis* is that the observed shear bands in Fig. 1(c) arise from intermediate necking with the inclination angle being governed by geometric aspect ratio and loading biaxiality. This paper aims to investigate the role of several key factors on the origin and layout of "shear bands" on the surfaces of layered heterostructured materials, including perturbation wavelength, aspect ratio of the specimen cross-section, high-*N* inner layer and low-*N* outer layer thickness ratio, and inclination angle of the perturbation. Our previous work has investigated the influence of these factors on uniform ductility and provided a theoretical foundation based on the Hutchinson-Neale criterion (Wang et al., 2021). But this prior work involves numerical simulations with plane strain conditions; in other words, the default model width is infinite, which thus lacks the investigation on thickness and the evolution of "shear bands" on the low-*N* outer layer surface. The simulation results will also reveal the shear band arrangement dependence on the geometric factors of the perturbation, and the whole evolution of the shear band arrangement. Studies presented in this work will allow us to compare to recent literature experiments (Yuan et al., 2019; Wang et al., 2019; Wang et al., 2020; Wang et al., 2020). Our findings will provide new ideas for the study of "shear bands" from continuum mechanics point of view, and also give design strategies for further engineering applications of layered heterostructured materials. While most previous studies focused exclusively on the back stress and GND, their employed processing techniques such as rotationally accelerated shot peening (RASP) and piezoelectric surface nano-crystallization (PSNC) greatly affect the material surface roughness (Wang et al., 2017; Li et al., 2017), which can nevertheless be considered as a key factor governing the necking mode.

The *second hypothesis* of this work aims to offer an alternative or complementary explanation to the enhanced ductility in layered heterostructured materials. Key ideas are borrowed from a design in flexible electronics by Li, Suo, and others (Wang et al., 2021; Li et al., 2004; Li et al., 2005; Xiang et al., 2005; Li and Suo, 2006; Lu et al., 2010; Jia and Li, 2013; Jia and Li, 2019), as illustrated in Fig. 1(f). Referring back to Fig. 1(e), the metal thin film behaves like the lower curve because of the lower *N*, while the polymeric substrate (or inner layer) behaves like the upper curve with a higher *N*. For the free-standing metallic material with arbitrary surface perturbations, the longest wavelength one will correspond to the lowest critical strain for necking to grow. The critical strain, being equal to *N* in this Considère mode, is low. Correspondingly, it is commonly found that a free-standing metal film has limited ductility. Taking advantage of the constraining effect of polymer substrate on the evolution of local strain, the ductility of metal film can be considerably improved (Xiang et al., 2005; Lu et al., 2010; Macionczyk and Brückner, 1999). Let us consider a random surface perturbation with a wide range of wavelengths on the surface of film/substrate or sandwich structure in Fig. 1(f). A long-wavelength perturbation will actually lead to a deformation field mostly localized in the inner-layer high-*N* material, so the uniform ductility reaches N_{soft}. An ultra-short-wavelength perturbation, just like the Rayleigh surface wave, only leads to nonuniform deformation in the low-*N* outer layer, so that the uniform ductility reaches $\sqrt{N_{hard}/2}$. Both limit cases have ductility levels that are higher than the low-*N* material in the free-standing state. Such a ductility enhancement methodology does not require the additional strengthening by GND or HDI. It arises purely from multiple unstable deformation modes.

From the above discussion, it is our premise that the experimentally observed dispersive shear bands in Fig. 1(c) may correspond to the selection of intermediate-wavelength necking mode, which in turn lead to a novel ductility-improvement strategy. Neither of these two above-mentioned hypotheses requires the microscopic mechanisms that involve GND or others. Our present work therefore aims to provide a comprehensive theoretical and numerical study to validate this new perspective.

2. Model setup

Here, we employ the simplified 3D layered heterostructured model in Abaqus to simulate the tensile process under the influence of surface perturbations, establish a relationship between ductility and "shear band" morphology by analyzing the surface strain field evolution on the surface of the low-*N* outer layer, and explain the inclination angle of the normal of "shear band" to the tensile axis. The model setup process is as follows: (a) Geometric modeling: A Python script file is utilized to generate sinusoidal curves with varying wavelengths and amplitudes (specifically, in this study, the amplitude is varied according to the relative amplitude $2\delta/t_{total}$, with values of 0.04 cm and 0.004 cm). By employing mirror and line tools, the width (w) of 4 cm and length (L) of $n \times \lambda+\lambda/2$ (i.e., n is an integer, and L is the length of the sinusoidal curve) are delineated. The basic stretching tool is then employed to transform the curves into rectangular prisms with a thickness of t_{total} (where t_{total} varies with cross-section ratio). The geometry is divided into a three-layer laminated structure with a low-N/high-N/low-N arrangement using the geometry splitting tool. Moreover, the α angle is generated by rotating the wavevector angle. (b) Material properties: The simplified isotropic power-law hardening UHARD subroutine is implemented, as will be given in Eq. (4). The finite deformation is adopted. (c) Boundary conditions: The left edge of the bottom layer of the laminated structure is fixed in the x-direction displacement. One corner along this edge is fixed in the y-direction displacement. The bottom surface exhibits fixed displacement in the z-direction, while a displacement in the positive Z-axis direction is applied to the top surface. Furthermore, the shear deformation in the xy plane has a minimal influence on the uniaxial tensile process. (d) Mesh generation: The geometric models are uniformly meshed into hexahedral structures with an approximate global size of 0.003. The element type employed is C3D8R, representing three-dimensional stress state. As shown in Fig. 2, the layered heterostructured material consists of low-*N*/high-*N*/low-*N* layers in a sandwich arrangement. The loading direction, boundary conditions, and geometric parameters are clearly labeled, from which we can define the following dimensionless parameters,

$$\frac{t_{soft}}{t_{total}},\ \frac{2\delta}{t_{toatl}},\ \frac{1}{2}kt_{total},\ \frac{t_{total}}{w} \tag{3}$$

where t_{total} is the thickness of the whole model, t_{soft} is the high-*N* inner layer thickness, δ is the amplitude of the sinusoidal perturbation on the surface as shown in Fig. 2(c), k is the wavenumber of the sinusoidal wave (i.e., the wavelength $\lambda=2\pi/k$), and w is the width of the model as shown in Fig. 2(d)). This work only studies two $2\delta/t_{total}$ values: 0.01 and 0.001. The latter requires a very fine mesh in order to faithfully capture the nonuniform deformation fields. As shown in Figs. 2(e) and (f), the inclination of the wave vector direction to the loading axis is described as α, or equivalently, it is equal to the angle between the "shear band" and the horizontal axis, which is π/2-α. Additionally, this work also studies the role of a phase shift, θ, of 180° (i.e., the perturbation on one side is panned 180° in z-axis relative to Fig. 2(b)).

A power-law hardening model is adopted here for the materials (Wang et al., 2021), given by

$$\varepsilon = \begin{cases} \sigma/E \ \sigma \le \sigma_y \\ \dfrac{\sigma_y}{E}\left(\dfrac{\sigma}{\sigma_y}\right)^{1/N} \quad \sigma > \sigma_y \end{cases} \tag{4}$$

here σ_y is the yield strength, and *E* is young's modulus. Isotropic hardening and associated J_2 flow are used. To avoid studying too many unimportant parameters, the high-*N* and low-*N* materials are assumed to have the same Young's modulus and Poisson's ratio. We focus on the different work hardening exponents in these two types of layers, as denoted as ideal material in Table 1. To compare with experiments in (Wang et al., 2020), we have curves fitted to their experimental stress-strain curves of nanocrystalline and coarse-grained materials, and then obtain the parameters as the actual material in Table 1. As will be shown later, the *N* values play much higher importance than other material properties. It is important to note that our simulations are performed on the entire model.

3. Finite element simulation results

To study the effects of wavelength ($0.5kt_{total}$), initial relative amplitude ($2\delta/t_{total}$), section ratio (t_{total}/w), high-*N* inner layer thickness (t_{soft}/t_{total}), and inclination angle (α) during uniaxial stretching, layered heterostructured models with surface perturbation of varying wavelengths were developed as shown in Fig. 2. It is necessary to point out that the perfect interface is assumed between the two materials.

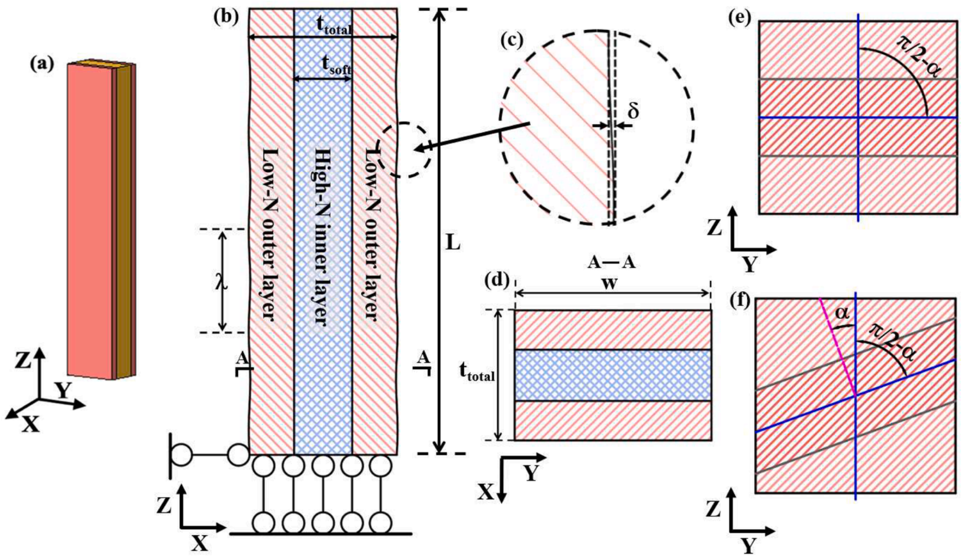

Fig. 2. Schematic illustration of the model setup for layered heterostructured materials with different $0.5kt_{total}$. The red region represents the hard material (low-N outer layer), and the blue one represents the soft material (high-N inner layer). (a) The 3D schematic with the labeled coordinates. (b) The XOZ section diagram of the sample with the ratio between t_{soft} and t_{total} ranging from 0 to 1, along with varying the wavelength by adjusting λ. (c) The enlarged image of the sinusoidal perturbations on the surface of the sample, while changing $2\delta/t_{total}$ results in amplitudes at 0.01 or 0.001. (d) The XOY section diagram at A-A of (b), with adjustable cross-section aspect ratio. (e) Schematic diagram of the sinusoidal perturbation with wavevector aligned int the tensile direction. (f) Corresponding perturbation with an inclination angle of α.

Table. 1
Material parameters used for the high-*N* inner and low-*N* outer layers. The actual materials are based on curve fitting to the stress-strain responses in (Wang et al., 2020).

	Materials	Young's modulus	Poisson's ratio	Yield strength	Work hardening exponent
Ideal Case	high-N inner Layer	90 GPa	0.3	400 MPa	0.2
	low-N outer Layer	90 GPa	0.3	400 MPa	0.02
Actual Experiment	high-N inner Layer	91.5 GPa	0.3	68 MPa	0.47
	low-N outer Layer	91.5 GPa	0.3	397 MPa	0.15

3.1. Deformation response when the wavevector is parallel to the tensile axis (α=0°)

Fig. 3 shows the engineering stress-strain curves and the relative amplitude change vs. engineering strain curves for layered heterogeneous materials. The final ductility is determined by intercepting the extrapolated dashed line with the horizontal axis (Wang et al., 2021), as shown in Fig. 3(a). This is justified because there is no failure process in the fintie element model, while the end tail of the stress-strain curve is a numerical artifact of severely elongated mesh in the neck zone. Furthermore, the relative amplitude change curve is plotted by tracing the surface morphology changes (i.e., tracing a trough with respect to its initial position), and the uniform ductility is determined by the intersection of two extrapolated bilinear dashed lines as shown in Fig. 3(b). Determining the uniform ductility based on the maximum stress only works when $2\delta/t_{total}$=0, while the use of amplitification factor in Fig. 3(b) corresponds to the Marciniak-Kuczyński method in forming limit anlaysis (Hutchinson and Neale, 1977; Marciniak and Kuczyński, 1969). From Fig. 3, both uniform ductility and final ductility display a trend of increasing and then decreasing when $0.5kt_{total}$ ranged from 0 to 2.0, while a weak increasing trend appears after $0.5kt_{total}$ exceeds 2.0. The tensile strength of the materials with different $0.5kt_{total}$ value has not shown a significant change, which again indicates the difficulty in determining uniform ducitlity from these near-flat maxima. Meanwhile, the corelation between $0.5kt_{total}$ value and the maximum ductility will also be affected by various factors (e.g., t_{total}/w = 1.0 and α=0°), with more details to be discussed shortly.

The dependence of final and uniform ductility with respect to increasing $0.5kt_{total}$ value at different cross-section aspect ratios are shown in Fig. 4(a). As the $0.5kt_{total}$ increases, both ductility measures show a trend toward increasing, decreasing, and then increasing, but the critical point for maximum ductility appears at different $0.5kt_{total}$ value (e.g., when t_{total}/w = 1, the maximum ductility occurs at $0.5kt_{total}$=1). From a visual inspection, the wavelengths can be classified into three regions: long wave region (i.e., $0.5kt_{total}$ =0~0.5), intermediate wave region (i.e., $0.5kt_{total}$=0.5~1.5), and short wave region (i.e., $0.5kt_{total}$=1.5~3.0). In the long wave region, the ductility increases almost linearly and tends to rise dramatically with the decreasing t_{total}/w. In the intermediate wave region, the ductility increase as t_{total}/w decreases, but an early drop in ductility occurs when t_{total}/w reaches 0.4. In other words, a change in the cross-section aspect ratio is likely to affect the ductility regions identified by the short and intermediate waves, which have less sensitivity to α values at 0° compared to other inclination angles. Compared to Fig. 11, t_{total}/w in Fig. 4(a) needs to be reduced to a very small value (i.e., decrease in t_{total}/w from 1.0 to 0.4) in order to change the wavelength region, otherwise it only changes the level of ductility. In the α=50° case, even a mere reduction of t_{total}/w from 1.0 to 0.7 results in a significant change in the wavelength region, and the above phenomenon is attributed to the fact that an inclination angle greater than 0° makes the jump in the necking critical condition more sensitive. It should be noted again that the multiple peaks/troughs Fig. 1(d) from theoretical predictions can only be seen if $2\delta/t_{total}$ approaches zero. After the dramatic change in long wave and medium wave regions, ductility curve flattens asymptotically in the short-wave region and only increases slightly with decreasing t_{total}/w. The synergistic effect of wavelength and cross-section aspect ratio could be further illustrated in Fig. 4(b). It can be seen that ductility remains monotonically increasing with decreasing t_{total}/w at short and long waves (e.g., $0.5kt_{total}$=0.1 and $0.5kt_{total}$=3.0). When $0.5kt_{total}$ ranges from 0.5 to 1.0, the critical t_{total}/w value when ductility experiences a steep drop decreases with increasing $0.5kt_{total}$, which would thus correspond to the early drop of strain in the strain vs $0.5kt_{total}$ curve in Fig. 4(a). Some experimental works also show the impact of cross-section aspect ratio on ductility (Wang et al., 2021), but there is no explanation for the strain steep drop phenomenon. Results here shed insights on this observation and will be discussed in details shortly. Overall, it can be concluded that choosing appropriate cross-section ratio and intermediate wavelength can result in a significant improvement in ductility (e.g., the case with $0.5kt_{total}$=1 and t_{total}/w = 0.6).

Fig. 5 shows the influence of high-*N* inner layer thicknesses on uniform ductility under different wavenumbers. The effect of wavelength on ductility shows similar trends as in Figs. 3 and 4. It can also be found that ductility increases with increasing high-*N* inner layer thickness, which benefits from the high-*N* inner layer being able to effectively limit the propagation of the "shear bands" (Wang et al., 2020). Additionally, it once again shows that smaller amplitude and suitable phase differences are preferable in improving the ductility. Results in Figs. 4 and 5 provide a synergistic enhancement of deformation heterogeneity and its evolution into dispersive shear bands, but the origin and selection of the wavelength in the literature (Li et al., 2020; Zhu and Wu, 2022; Wan et al., 2021; Jiang et al., 2022; Yuan et al., 2019; Wang et al., 2019; Wang et al., 2020; Wang et al., 2020) have not been studied.

3.2. Deformation response when the wave vector makes an acute angle to the tensile axis

The effect of α on the ductility of the perturbation model is studied in this subsection. In literature works, the angle of the "shear bands" (i.e., distribution in YOZ plane, as shown in Fig. 2) are reported to range from 45° to 50° (Yuan et al., 2019; Wang et al., 2019; Wang et al., 2020; Wang et al., 2020), and the method similar to the forming limit diagram is used here to form an inclined "shear band" by adjusting the inclination angle (Marciniak and Kuczyński, 1969; Wang et al., 2011; Srivastava et al., 2016). As shown in

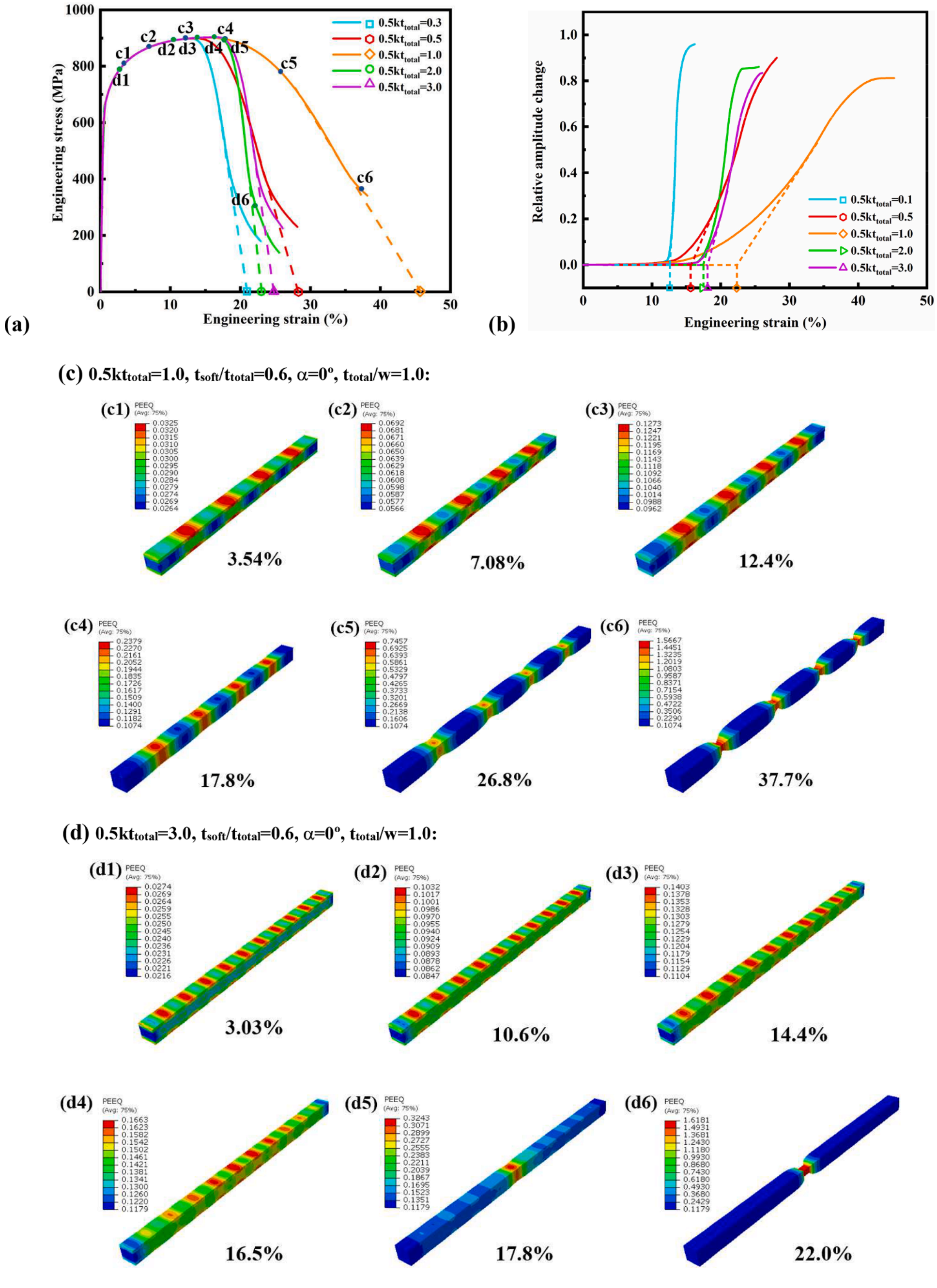

Fig. 3. The effect of the surface perturbation on uniform ductility and final ductility for t_{total}/w, t_{soft}/t_{total}, $2\delta/t_{total}$ and α are equal to 1, 0.6, 0.001, and 0°, as well as employing ideal material parameters. (a) The engineering stress-strain curves with representative $0.5kt_{total}$, and the final ductility determined from extrapolation. (b) Relative amplitude change curve with increasing engineering strain, the uniform ductility obtained by Hutchinson-Neale criterion (i.e., uniform ductility is determined from the intersection point by plotting double tangents to the sudden increase in harmonic perturbation (Hutchinson and Neale, 1977; Wang et al., 2021)). See the text for the basic principles of extrapolation of the dashed line. (c) The three-dimensional contour plot of the equivalent plastic strain during the uniaxial tensile process, where $0.5kt_{total}$=1.0, corresponds to the points along the orange curve in Fig. 3(a). (d) The three-dimensional contour plot of the equivalent plastic strain during the uniaxial tensile process, where $0.5kt_{total}$=2.0, corresponds to the points along the green curve in Fig. 3(a).

Figs. 6(a) and (b), the effects of inclination angle and wavelength on ductility are investigated by fixing $0.5kt_{total}$ and α value separately. Compared to the horizontal “shear bands” in Fig. 4(b), similar trend could be found at α=50° when increasing t_{total}/w, but the critical points for the steep drop are delayed, as illustrated in Fig. 6(a). Meanwhile, the inclination of the wave vector direction to the stretching axis weakens the ductility, i.e., the ductility is maximum at α=0°, and it decreases as the inclination angle increases. The

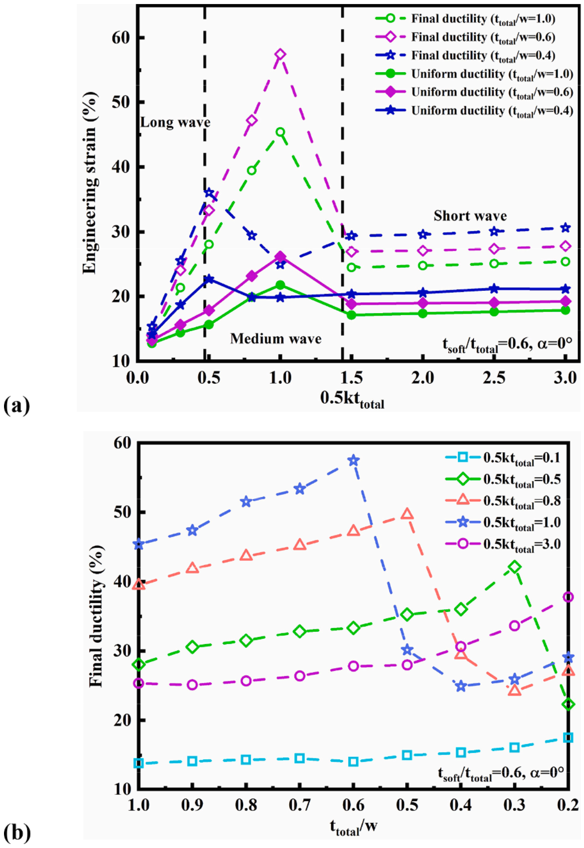

Fig. 4. Synergistic effect of wavelength and cross-section aspect ratio on ductility. (a) The curve of engineering strain versus wavelength with different t_{total}/w, where the wavelength can be divided into three regions of long, intermediate, and short values, and the t_{total}/w value may alter these regions. (b) The final ductility with t_{total}/w and $0.5kt_{total}$. The steep drop in ductility corresponds to the change in the wavelength region as shown in (a). All these simulations correspond to t_{soft}/t_{total}=0.6, $2\delta/t_{total}$=0.01, and α=0°. Moreover, ideal material parameters in Table 1 are used.

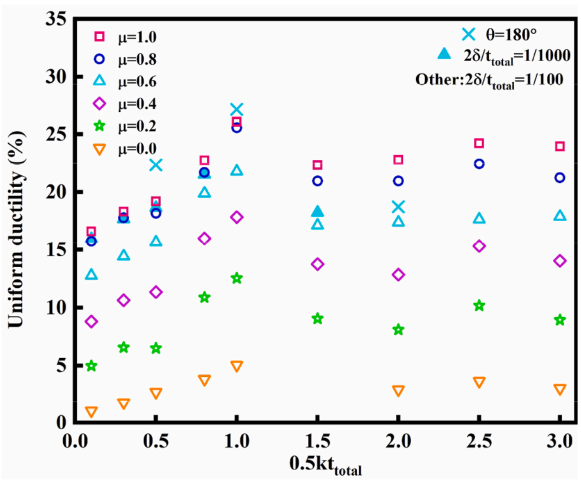

Fig. 5. Synergistic effect of wavelength and high-N inner layer thickness on uniform ductility with $2\delta/t_{total}$=1/100, t_{total}/w = 1.0 and α=0°, except for filled symbol and blue forks which correspond to $2\delta/t_{total}$=0.001 and θ=180° (i.e., the sinusoidal perturbation on the back surface produces a phase difference in 180° with respect to that on the front surface), respectively. Ideal material parameters in Table 1 are used.

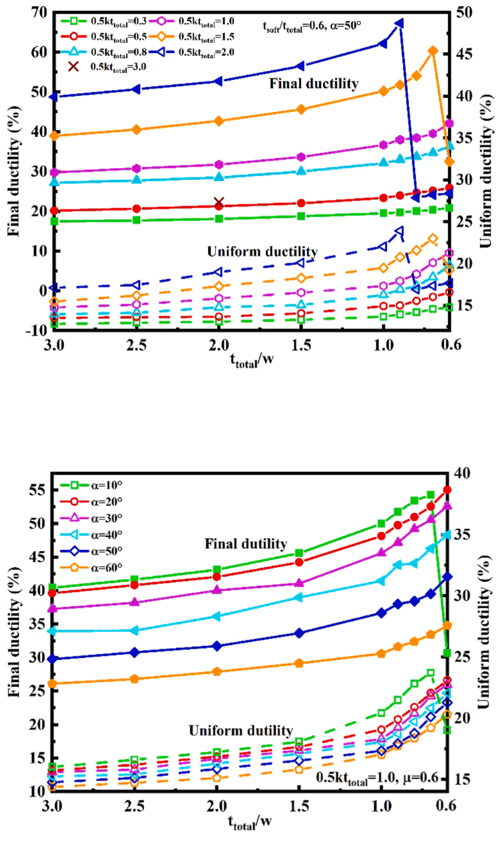

Fig. 6. (a) With a fixed α=50°, the role of the cross-section aspect ratio and the wavelength on the ductility is investigated, which shows a similar trend to Fig. 4(b). (b) The clear indication that the inclination angle change has an effect on the elongation at $0.5kt_{total}$=1.0. Additionally, the sudden jump in both figures is due to the transition of various wavelength regions with respect to t_{total}/w and α, as shown also in Fig. 8(a). The calculations in the figure use ideal material parameters in Table 1.

reason for the above phenomenon is that the projection length of the wave on the XOZ plane has increased due to the inclination angle (i.e., this corresponds to an increase in wavelength, while the "shear bands" in the XOZ plane will rotate during tension). The effect of inclination angle on ductility can also be seen in Fig. 6(b). The observation for the steep drop of strain in Fig. 6 is consistent with results

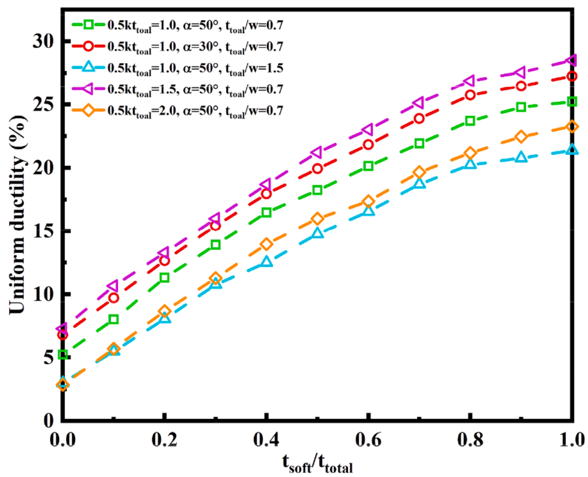

Fig. 7. The influence of increasing soft layer thickness on uniform ductility with the representative combination of $0.5kt_{total}$, α, t_{total}/w. The calculations in the figure use ideal material parameters in Table 1.

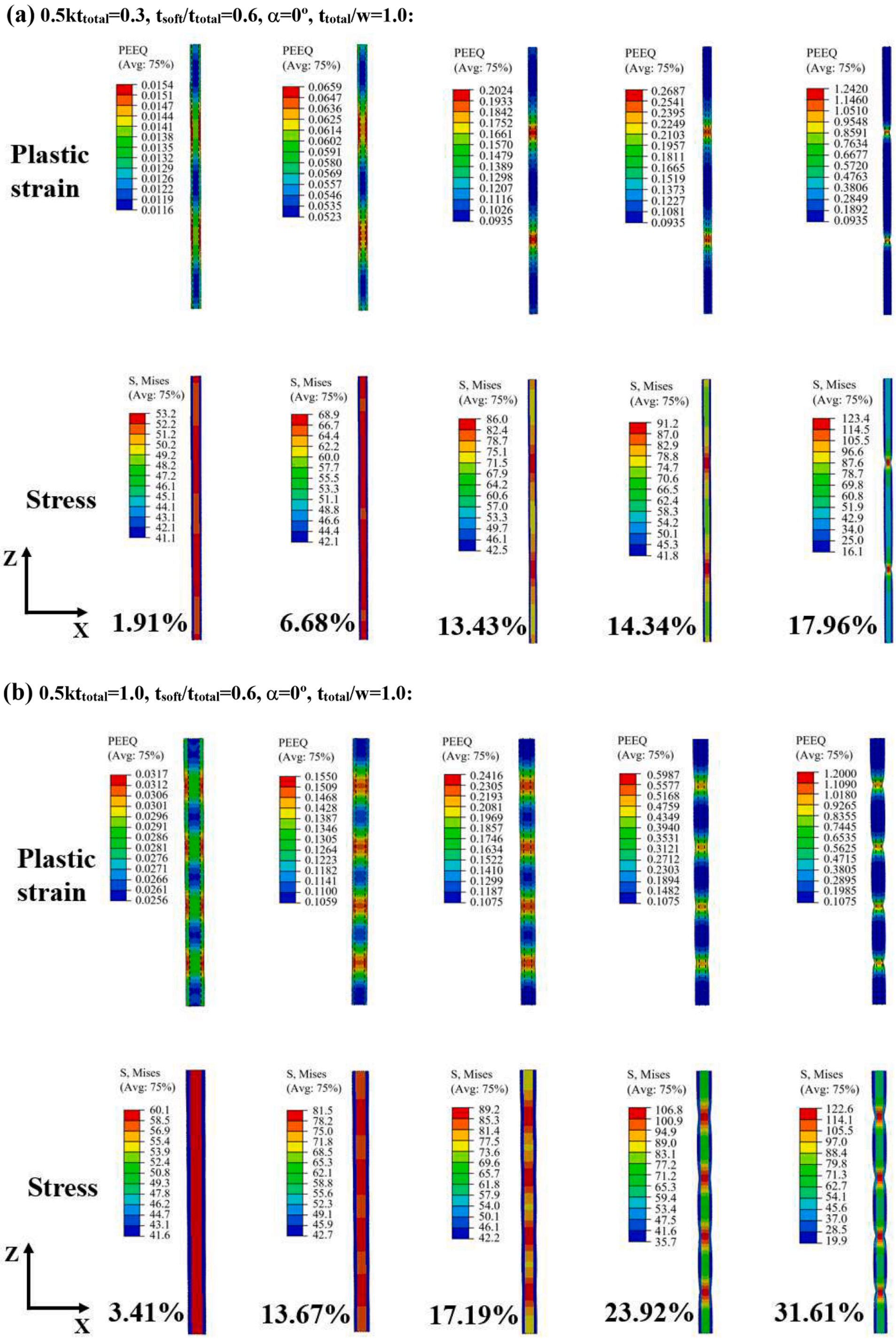

Fig. 8. Contour plots of the plastic strain and stress distributions for the case of the long wave, intermediate wave, and short wave with increasing engineering strain. (a) $0.5kt_{total}=0.3$, $t_{total}/w=1$, $t_{soft}/t_{total}=0.6$, $2\delta/t_{total}=1/100$ and $\alpha=0°$. (b) $0.5kt_{total}=1.0$, $t_{total}/w=1$, $t_{soft}/t_{total}=0.6$, $2\delta/t_{total}=1/100$ and $\alpha=0°$. (c) $0.5kt_{total}=3.0$, $t_{total}/w=1$, $t_{soft}/t_{total}=0.6$, $2\delta/t_{total}=1/100$ and $\alpha=0°$. (d) $0.5kt_{total}=3.0$, $t_{total}/w=1$, $t_{soft}/t_{total}=0.6$, $2\delta/t_{total}=1/100$, $\alpha=0°$ and $\theta=180°$ (i.e., details explained in Fig. 5). The morphology of the XOZ surface is plotted. The above calculations use ideal material parameters in Table 1. Dashed line represents the high-N inner layer, while the region outside the dashed line corresponds to the low-N outer layer. It should be noted that the plastic strain shown in the figure represents the equivalent plastic strain obtained by subtracting the elastic strain from the total strain.

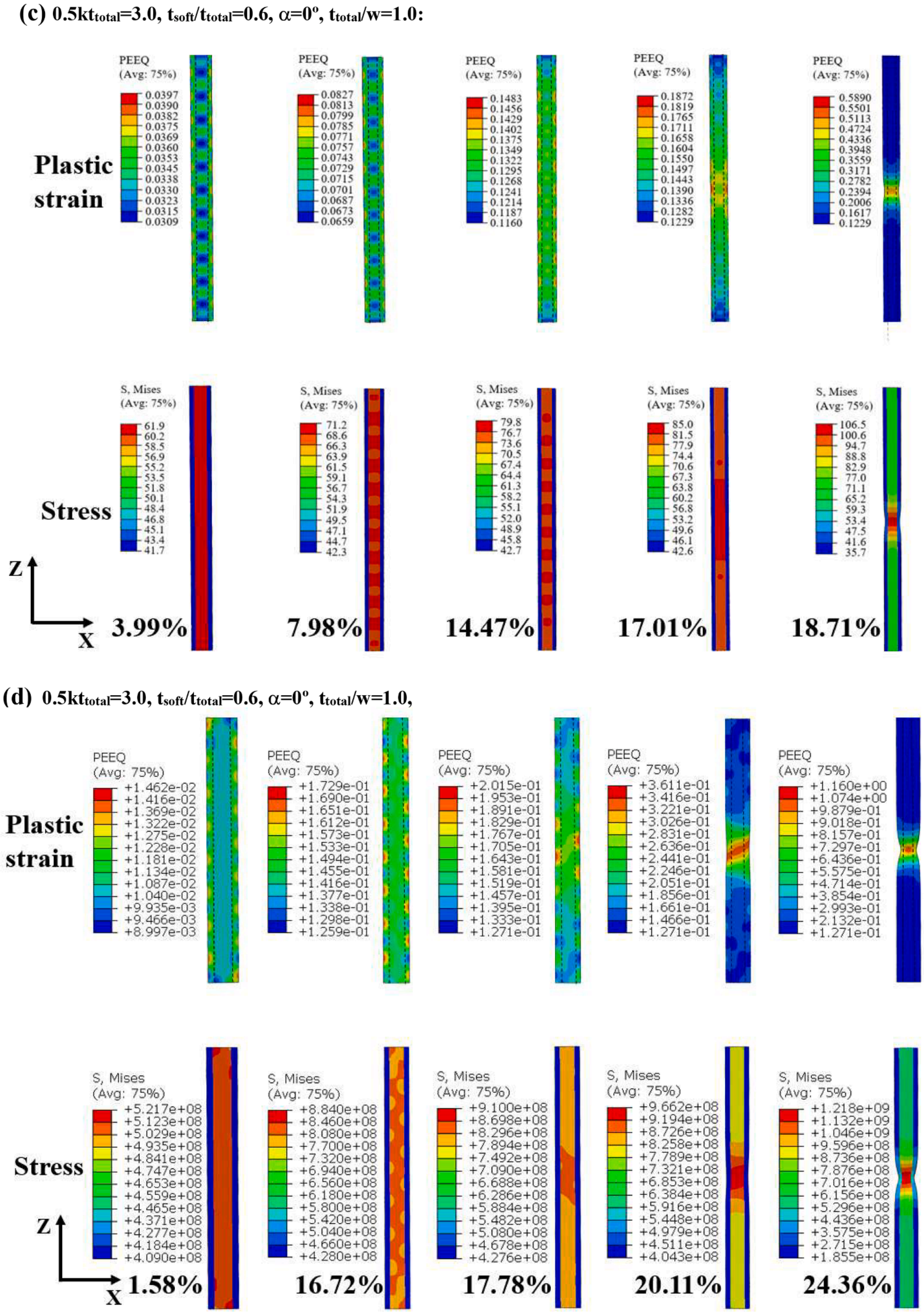

Fig. 8. (*continued*).

in Fig. 4.

In previous studies, the thickness of the low-*N* outer layer and high-*N* inner layer have also been regarded as important factors in affecting ductility (Xiang et al., 2005; Li and Suo, 2006; Lu et al., 2010), and the reason for the ductility enhancement is generally considered as a result of the constrains on local necking in high-*N* inner layer or the “shear bands” in low-*N* outer layer which prevent the early instability. The dependence of ductility on t_{soft}/t_{total} under different conditions has been shown in Fig. 7, all curves appear to remain monotonically increasing along with t_{soft}/t_{total} increase from 0 to 1, which again demonstrates that the ductility could be weakened by the inclination angle. Furthermore, uniform ductility jumping from the Considère criterion to the Rayleigh criterion at specific t_{soft}/t_{total} values, which may explain the surprising ductility of t_{soft}/t_{total} over 0.6 (Wang et al., 2020). Additional discussions on inclination angle selection and “shear band” evolution will be provided later.

4. Discussions and experimental comparisons

4.1. Evolution of "shear band" or necking arrangements

One barrier to explore the causes and influences of shear band formation lies on the difficulty in observing the entire evolution of their arrangement. Here we provide a systematic investigation along this line for our layered heterostructured materials with different morphological perturbations in Fig. 2, based on both the strain contour plots and the stress contours plots in Figs. 8 and 9. In Fig. 8, with loading strain increasing, for the $0.5kt_{total}$=0.3 case, the strain in the z-direction cannot be dispersed and the "shear bands" rapidly penetrates the model along the X and Y directions, and early necking occurs. For the $0.5kt_{total}$=3.0 case, the strain can be uniformly dispersed into multiple "shear bands" during the pre-loading stage, and a single neck appears, resulting in a more concentrated strain in z-direction and leading to a rapid failure. However, the corresponding resistance of nonuniform deformation behavior for the $0.5kt_{total}$=1.0 case is superior, as no premature localized necking occurs and more significant Rayleigh-type characteristics are shown in these intermediate wave perturbation case under the same loading conditions, as shown in Fig. 8(b). Again, these results confirm the ranking of the effects in perturbation-enhanced ductility as: intermediate wave > short wave > long wave. Furthermore, the phase difference of the perturbation also plays a role in delaying the formation of the localized necking as show in Fig. 8(c) and (d). All of material deformation in these simulations start with "shear band" spreading, followed by the appearance of diffuse and localized necking, so that the morphological evolution of the "shear band" plays a crucial role in ductility. These "shear bands" are perpendicular to the direction of the tension axis when either the intermediate wave perturbation in Fig. 8(b) or the long wave perturbation in Fig. 8(a) is applied in the model. Compared with the long wave cases, intermediate wave cases distribute the deformation in the cross-sectional direction evenly with more necks, which is responsible for the enhanced ductility. These results suggest that the structure of the perturbations plays a critical role in the arrangement of the "shear bands", consistent with experimental findings such as in (Wang et al., 2020). Meanwhile, the previous work has attributed the main factor which will affect the shear band arrangement to sample thickness, but our work found that the cross-section aspect ratio is merely one of many factors affecting "shear band" arrangement, rather than the only factor. Besides, this work also found that the "shear bands" first formed in the low-*N* outer layer and then continuously propagate to the high-N inner layer until the whole model is penetrated, and similar results could be found in the previous experiments (Wang et al., 2020).

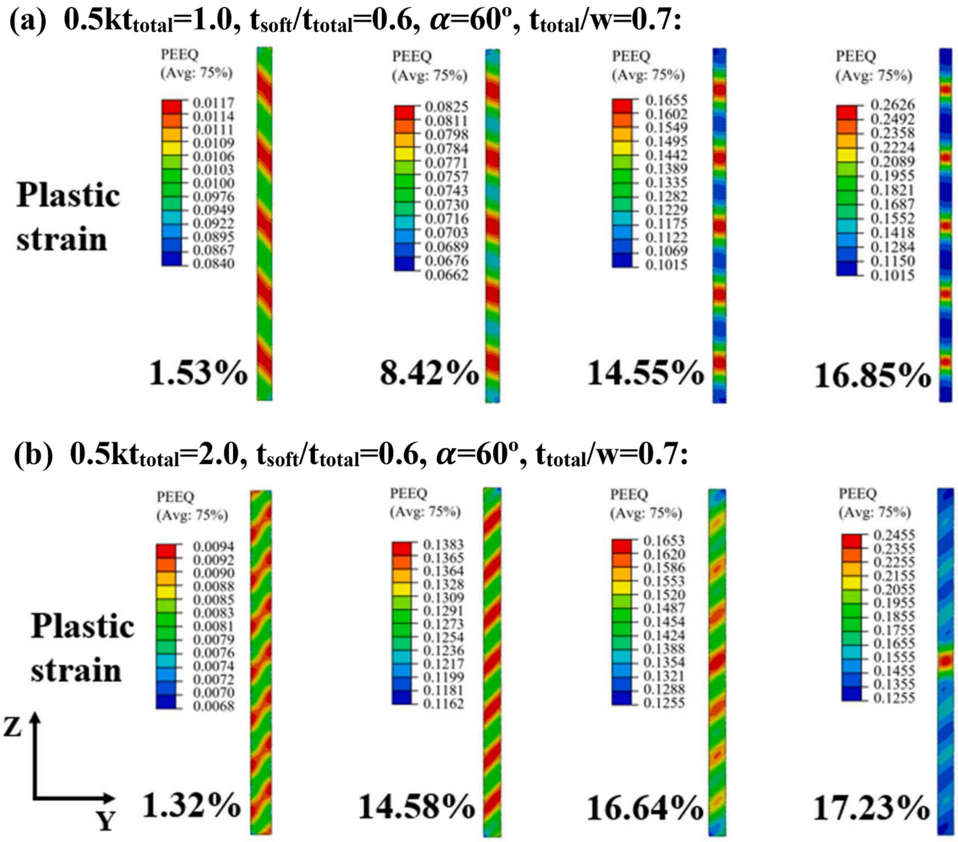

Fig. 9. The plastic strain contour plots for the case of the intermediate wave and short wave with increasing engineering strain in the XOY plane. (a) $0.5kt_{total}$=1.0, t_{total}/w = 0.7, t_{soft}/t_{total}=0.6, $2\delta/t_{total}$=1/100 and α=60°. (b) $0.5kt_{total}$=2.0, t_{total}/w = 0.7, t_{soft}/t_{total}=0.6, $2\delta/t_{total}$=1/100and α=60°. The above calculations use ideal material parameters in Table 1.

The strain fields in the YOZ plane are shown in Fig. 9, illustrating the deformation behavior and shear band arrangement with different inclination angles. In both the intermediate-wave and short-wave cases, the shear band rotates toward the vertical tensile axis as the macroscopic strain increases. The difference lies in the short-wave cases, where multiple necks eventually evolve into a single neck as shown in Fig. 9(b).

Results from Figs. 8 and 9 can be summarized into the evolution of shear band arrangements in Fig. 10, including I-type, X-type, and W-type. Note the change of the viewing plane from XOZ to YOZ for the bottom right figure there. In the short-wave case, X-type "shear band" is observed, while the phase difference of 180° to one side form W-shaped "shear band". The formation of the three types of "shear bands" can be attributed to stress concentration induced by disturbances, which in turn induce the extension of strain bands along a specific direction. The I-type strain band is formed due to the relative alignment of two troughs and the longer wavelength, resulting in the extension of the strain band along the X direction. When $\theta = 180°$, the misalignment between the peaks and valleys on the upper and lower surfaces of the YZ plane, as well as the phase difference between the positions of the two strain clusters, ultimately lead to the formation of the W-shaped strain band. On the other hand, the overlapping of stress fields caused by ultra-short wavelengths results in the formation of intersecting strain bands, namely the X-type.

4.2. Surface perturbation and wavelength selection

Clearly, the initial perturbation is random and has a wide range of wavelengths. The selection of some certain wavelengths is further investigated here by the ductility diagrams under different factors in Figs. 11 and 12, as well as the plastic strain contour plots in the previous subsections.

The same trend has been found in Fig. 11 as in Fig. 4(a), i.e., ductility measures increase and then decrease with respect to the decrease of the wavelength. The representative parameters in this figure reveal the effect of the cross-section aspect ratio (t_{total}/w), the inclination angle (α), and the high-*N* inner layer thickness (t_{soft}/t_{total}) on the transition of long/intermediate/short wavelength regions. As the value of t_{total}/w increases, the intermediate wave region continues shifting to the right, with smaller t_{total}/w values having better

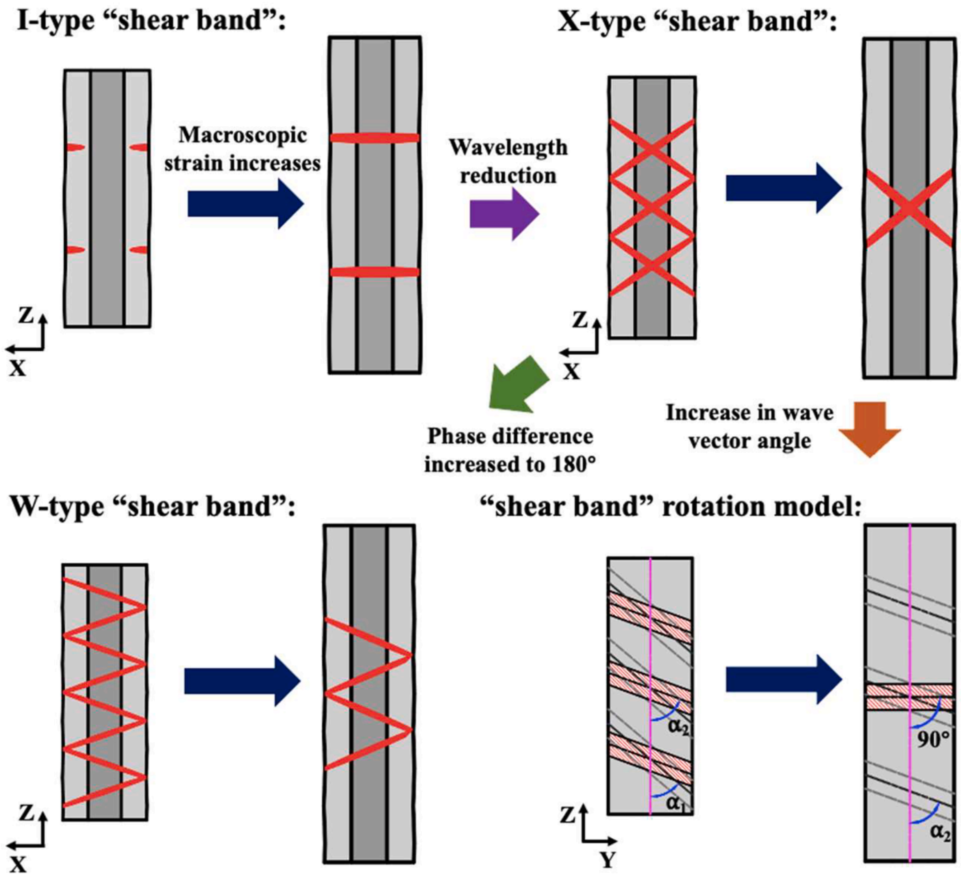

Fig. 10. Schematic diagram showing the evolution of the "shear band" in the surface perturbation model during tension. The red line is the "shear band" due to the present deformation and is updated when further distortion occurs, while the red diagonal region in the XOZ plane is the "shear band". The evolution of the "shear bands" with type I, X, and W is the result of the surface perturbation morphology in the XOZ plane. In addition, the "shear band" is rotated in the YOZ plane with an inclination.

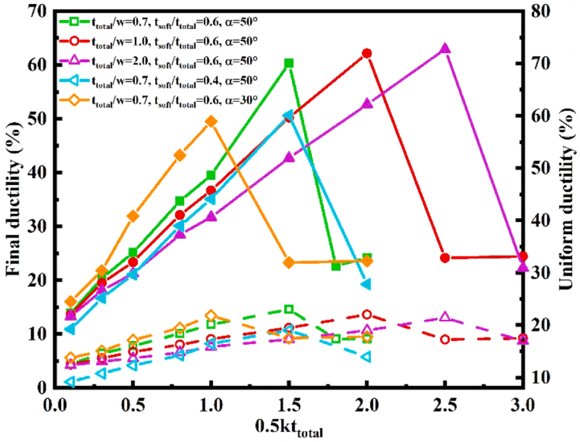

Fig. 11. The combined effect of $0.5kt_{total}$, t_{total}/w, t_{soft}/t_{total} and α on ductility is shown to have a more significant sensitivity compared to the wavelength range in Fig. 4(a). It should be noted that the calculations in this figure use ideal material parameters in Table 1.

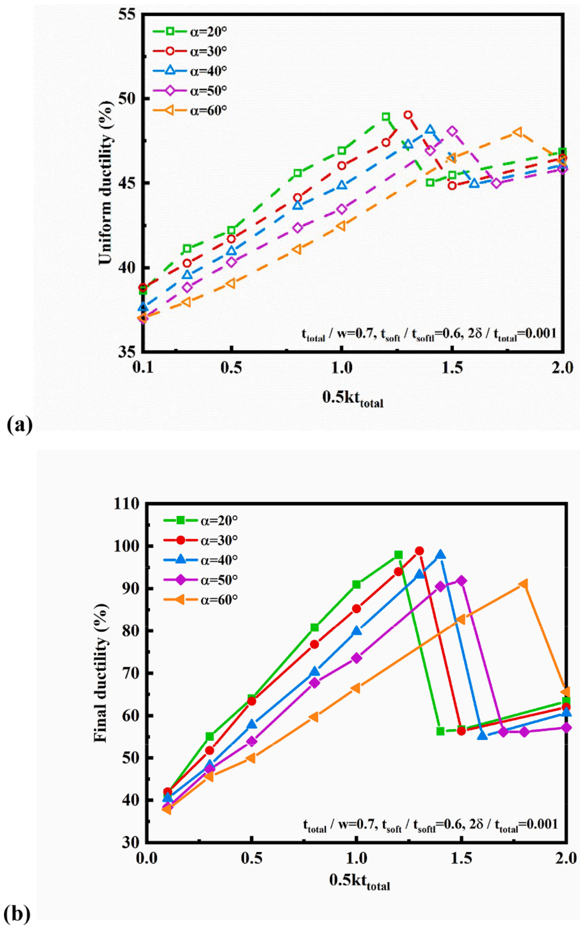

Fig. 12. Simulation results using the actual material parameters in Table 1, based on experimental calibration with Ref. (Wang et al., 2020; Wang et al., 2020). Under random perturbations, the necking condition is determined by the minimum value of the uniform ductility (e.g., the sample surfaces with perturbation of $0.5kt_{total}$=0.3, 0.8, 1, then necking occurs according to uniform ductility of $0.5kt_{total}$=0.3, as shown in Fig. 3). (a) Uniform ductility. (b) Final ductility.

ductility before the ductility drops. Some experimental works show consistent results (Wang et al., 2020), which attribute the increase in ductility to the evolution of the morphology and number of shear bands generated by the sample thickness. However, these literature studies are lack of a complete parametric investigation. The increasing value of α also has a similar trend to the region shift of t_{total}/w. In contrast to α and t_{total}/w, the effect of t_{soft}/t_{total} is only limited to the level of ductility rather than the dominant regions.

Results in Fig. 11 demonstrate the possibility of achieving high ductility in the intermediate wavelength region. First, referring back to observations in Fig. 1(c), it can be seen that the dispersive shear bands have a spacing on par with the sample cross-section sizes. Although perturbations at all wavelengths are possible, the prior sample preparation could lead to sample misalignment and nonuniformity in geometric features, all of which are on the macroscopic sample sizes. Obviously, one can easily validate this argument by preparing samples with given initial perturbations, which will be reported in our future work. Second, from results in Figs. 4–7, it can be seen that the longest wavelength necking gives the lowest ductility, so energetically, regardless of initial perturbations, shouldn't the Considère limit be selected? Along this line, we note that the selection of intermediate wavelengths can be due to a kinetic reason as shown by representative results in Fig. 3(b). In our sandwich structure, a long-wavelength perturbation does correspond to a lower critical strain, but the subsequent growth could be significantly retarded, because this perturbation falls into unstable condition of the low-*N* outer layer but actually into stable deformation mode of the inner high-*N* layer. The growth rate calculations like those in Fig. 3(b) indicate that intermediate-wavelength perturbations grow the fastest. Third, varying geometric parameters and also α, we can see the systematic shifts of the long/intermediate/short wavelength regions. For example, the family of ductility curves in Fig. 11 suggest that a small change of initial perturbation wavelength can lead to the sharp change of the selected inclination angle. Therefore, considering all the above factors, it is anticipated that the observed dispersive shear bands can be in a wide range of inclination angle (e.g., $20^\circ \sim 60^\circ$) and have a wide range of wavelengths (e.g., selection of $0.5kt_{total}$ in $1.7 \sim 2.0$ with $t_{total}/w = 0.7$).

Simulations thus far use the ideal material parameters in Table 1. Comparing to the experiments in (Wang et al., 2020; Wang et al., 2020) leads to a set of new material parameters in Table 1. Repeating our simulations, Fig. 12 illustrates the curve of uniform and final ductility with $0.5kt_{total}$ for different α values, from which it can be seen that the short-wave range is continuously delayed as α grows. Again, this diagram can be divided into three regions: long wave region ($0.5kt_{total}<1.1$), intermediate wave region ($1.1<0.5kt_{total}<2$), and short-wave region. The detrimental role played by the inclination angle on the ductility measures can again be seen in the long wave region. In the intermediate wave region, the strain decreases and the lowest strain values occur from $\alpha=20^\circ$ to 60°. This means that the "shear bands" tend to form at 20° to 60° (i.e., close to the maximum shear direction) in accord with experimental findings such as in Refs. (Yuan et al., 2019; Wang et al., 2019; Wang et al., 2020; Wang et al., 2020). These additional simulations suggest that the key factor that governs the shear bands and the enhanced ductility should be the large contrast between the work hardening rates of the low-*N* outer and high-*N* inner materials.

5. Conclusions

Heterostructured materials have exhibited enhanced strength and ductility, which are commonly understood from GND pileups and forward/back stresses on the microstructural length scales. In recent years, a number of works have found a peculiar observation of dispersive strain bands, especially on the surfaces of layered heterostructured materials. These bands are believed to be an effective way to redistribute the plastic deformation over a greater length scale and therefore to delay the progression of the deformation field into a major strain localization and then into failure. The work here now provides a mechanistic interpretation of these dispersive shear bands.

The major observations and results from our necking analysis and full-field numerical simulations include:

(1) Since the feature sizes are commensurate with the sample geometric sizes, GND and HDI are unlikely to be a major cause of these shear bands.
(2) Nonuniform deformation fields are a result of localized necking with variable wavelength. For a homogeneous material, the dependence of uniform ductility on the perturbation wavelength has been well established theoretically. For the layered structure, we rely on full 3D finite element simulations and conduct a complete parametric study.
(3) Dominant factors that help to improve the ductility of material includes: "shear band" arrangement, high-*N* inner layer thickness, initial amplitude, and cross-section aspect ratio. The "shear band" evolution could be controlled by adjusting the perturbation wavelength and phase difference.
(4) The evolutionary behavior of the shear bands shows three quintessential types, including I, X, and W types, which agree with the experimental observations, as summarized in Fig. 10.
(5) Of many possible random perturbations for the sandwich sample, the intermediate wavelengths are more likely to be selected due to the rapid growth rate. Simultaneously, the critical necking mode is very sensitive to geometric parameters, inclination angle, and material hardening rates, which explain the wide range of observations of the chosen wavelength and inclination angle in literature.
(6) These findings not only demonstrate that the essential reason for "shear band" formation in heterostructured materials, but also offer an innovative view on the ductility improvement.

Author Statement

All authors contribute equally to the conceptualization, execution, manuscript preparation and revision processes.

Data availability

Numerical simulation methodology and results are available upon communications to the corresponding authors.

Declaration of Competing Interest

The authors declare no competing interests.

Acknowledgments

Y. Zhao gratefully acknowledges the funding from National Natural Science Foundation of China (Grant No. 52061027), Science and Technology Program Project of Gansu Province (Grant No. 22YF7GA155, No. 22CX8GA109), Zhejiang Provincial Natural Science Foundation (Grant No. LY23E010002), and Hongliu Outstanding Talents Program of Lanzhou University of Technology (Grant 2018). X. Wang acknowledges the support from the Center for Materials Processing at the University of Tennessee.

References

Fang, T.H., Li, L.W., Tao, N.R., Lu, K., 2011. Revealing extraordinary intrinsic tensile plasticity in gradient nano-grained copper. Science 331, 1587–1590.
Gao, Y.F., Wang, L., Bei, H., Nieh, T.G., 2011. On the shear-band direction in metallic glasses. Acta Mater. 59, 4159–4167.
Hill, R., Hutchinson, J.W., 1975. Bifurcation phenomena in the plane tension test. J. Mech. Phys. Solids 23, 239–264.
Huang, C.X., Wang, Y.F., Ma, X.L., Yin, S., Hoppel, H.W., Goken, M., Wu, X.L., Gao, H.J., Zhu, Y.T., 2018. Interface affected zone for optimal strength and ductility in heterogeneous laminate. Mater. Today 21, 713–719.
Hutchinson, J.W., Neale, K.W., 1977. Influence of strain-rate sensitivity on necking under uniaxial tension. Acta Metall. 25, 839–846.
Jia, Z., Li, T., 2013. Necking limit of substrate-supported metal layers under biaxial in-plane loading. Int. J. Plast. 51, 65–79.
Jia, Z., Li, T., 2019. Bifurcation instability of substrate-supported metal films under biaxial in-plane tension. J. Mech. Phys. Solids 126, 52–75.
Jia, H.L., Wang, G.Y., Chen, S.Y., Gao, Y.F., Li, W.D., Liaw, P.K., 2018. Fatigue and fracture behavior of bulk metallic glasses and their composites. Prog. Mater. Sci. 98, 168–248.
Jiang, J.X., Chen, Z.K., Ma, H.C., Xing, H.Z., Li, X.Y., 2022. Strength-ductility synergy in heterogeneous-structured metals and alloys. Matter 5, 2430–2433.
Li, T., Suo, Z., 2006. Deformability of thin metal films on elastomer substrates. Int. J. Solids Struct. 43, 2351–2363.
Li, T., Huang, Z.Y., Suo, Z., Lacour, S.P., Wagner, S., 2004. Stretchability of thin metal films on elastomer substrates. Appl. Phys. Lett. 85, 3435–3437.
Li, T., Huang, Z.Y., Xi, Z.C., Lacour, S.P., Wagner, S., Suo, Z., 2005. Delocalizing strain in a thin metal film on a polymer substrate. Mech. Mater. 37, 261–273.
Li, J., Wang, G.J., Chen, S., Wu, X., 2017. On strain hardening mechanism in gradient nanostructures. Int. J. Plast. 88, 89–107.
Li, X.Y., Lu, L., Li, J.G., Zhang, X., Gao, H.J., 2020. Mechanical properties and deformation mechanisms of gradient nanostructured metals and alloys. Nat. Rev. Mater. 5, 706–723.
Lu, N.S., Suo, Z.G., Vlassak, J.J., 2010. The effect of film thickness on the failure strain of polymer-supported metal films. Acta Mater. 58, 1679–1787.
Lu, K., 2014. Making strong nanomaterials ductile with gradients. Science 345, 1455–1456.
Macionczyk, F., Brückner, W., 1999. Tensile testing of AlCu thin films on polyimide foils. J. Appl. Phys. 86, 4922–4929.
Marciniak, Z., Kuczyński, K., 1969. Limit strains in the processes of stretch-forming sheet metal. Int. J. Mech. Sci. 9, 609–620.
Needleman, A., 1988. Mateiral rate dependence and mesh sensitivity in localization problems. Comput. Methods Appl. Mech. Eng. 67, 69–85.
Rudnicki, J.W., Rice, J.R., 1975. Conditions for the localization of deformation in pressure sensitive dilatant materials. J. Mech. Phys. Solids 23, 371–394.
Srivastava, A., Bower, A.F., Hector Jr, L.G., Carsley, J.E., Zhang, L., Abu-Farha, F., 2016. A multiscale approach to modeling formability of dual-phase steels. Modell. Simul. Mater. Sci. Eng. 24, 025011.
Stören, S., Rice, J.R., 1975. Localizing necking in thin sheets. J. Mech. Phys. Solids 23, 421–441.
Wan, T., Cheng, Z., Bu, L.F., Lu, L., 2021. Work hardening discrepancy designing to strengthening gradient nanotwinned Cu. Scr. Mater. 201, 113975.
Wang, H., Wu, P.D., Boyle, K.P., Neale, K.W., 2011. On crystal plasticity formability analysis for magnesium alloy sheets. Int. J. Solids Struct. 48, 1000–1010.
Wang, X., Li, Y.S., Zhang, Q., Zhao, Y.H., Zhu, Y.T., 2017. Gradient structured copper by rotationally accelerated shot peening. J. Mater. Sci. Technol. 33, 758–761.
Wang, Y.F., Huang, C.X., He, Q., Guo, F.J., Wang, M.S., Song, L.Y., Zhu, Y.T., 2019. Heterostructure induced dispersive shear bands in heterostructured Cu. Scr. Mater. 170, 76–80.
Wang, Y.F., Huang, C.X., Li, Y.S., Guo, F.J., He, Q., Wang, M.S., Wu, X.L., Scattergood, R.O., Zhu, Y.T., 2020. Dense dispersed shear bands in gradient-structured Ni. Int. J. Plast. 124, 186–198.
Wang, Y.F., Huang, C.X., Li, Z.K., Fang, X.T., Wang, M.S., He, Q., Guo, F.J., Zhu, Y.T., 2020. Shear band stability and uniform elongation of gradient structured material: role of lateral constraint. Extreme Mech. Lett. 37, 100686–100691.
Wang, X., Li, T., Gao, Y.F., 2021. What really governs the upper bound of uniform ductility in gradient or layered materials? Extreme Mech. Lett. 48, 101413.
Wang, W.Y., Wang, Z.Q., Liang, Z.S., Xu, L., 2021. Effect of tensile–strain rate and specimen width on mechanical properties of cold-formed Q345 steel at elevated temperatures. J. Mater. Civ. Eng. 33, 04021218.
Xiang, Y., Li, T., Suo, Z.G., Vlassak, J.J., 2005. High ductility of a metal film adherent on a polymer substrate. Appl. Phys. Lett. 87, 161910–161913.
Yuan, F.P., Yan, D.S., Sun, J.D., Zhou, L.L., Zhu, Y.T., Wu, X.L., 2019. Ductility by shear band delocalization in the nano-layer of gradient structure. Mater. Res. Lett. 7, 12–17.
Zeng, Z., Li, X.Y., Xu, D.S., Lu, L., Gao, H.J., Zhu, T., 2016. Gradient plasticity in gradient nano-grained metals. Extreme Mech. Lett. 8, 213–219.
Zhang, W., Gao, Y.F., Feng, Z.L., Wang, X., Zhang, S.Y., Huang, L., Huang, Z.W., Jiang, L., 2020. Ductility limit diagrams for superplasticity and forging of high temperature polycrystalline materials. Acta Mater. 194, 378–386.
Zhao, H.Y., Liao, X.C., Cheng, S., Ma, E., Zhu, Y.T., 2006. Simultaneously increasing the ductility and strength of nanostructured alloys. Adv. Mater. 18, 2280–2283.
Zhu, Y.T., Wu, X.L., 2019. Perspective on hetero-deformation induced (HDI) hardening and back stress. Mater. Res. Lett. 7, 393–398.
Zhu, Y.T., Wu, X., 2022. Heterostructured materials. Prog. Mater. Sci. 131, 101019–101074.